

The OH Megamaser galaxy IRAS11506-3851: an AGN and star formation revealed by multiwavelength observations

C. Hekatelyne,^{1*} Rogemar A. Riffel,² Thaisa Storchi-Bergmann,¹ Preeti Kharb,³ Andrew Robinson,⁴ Dinalva Sales,⁵ Claudia M. Cassanta²

¹*Departamento de Astronomia, Universidade Federal do Rio Grande do Sul, 91501-970, Porto Alegre, RS, Brazil*

²*Departamento de Física, CCNE, Universidade Federal de Santa Maria, 97105-900, Santa Maria, RS, Brazil*

³*National Centre for Radio Astrophysics, Tata Institute of Fundamental Research, S. P. Pune University Campus, Post Bag 3, Ganeshkhind, Pune 411 007, India*

⁴*School of Physics and Astronomy, Rochester Institute of Technology, 84 Lomb Memorial Drive, Rochester, NY 14623, USA*

⁵*Instituto de Matemática, Estatística e Física, Universidade Federal do Rio Grande, Rio Grande 96203-900, Brazil*

Accepted XXX. Received YYY; in original form ZZZ

ABSTRACT

We present Gemini Multi-Object Spectrograph (GMOS) Integral Field Unit (IFU), Hubble Space Telescope (HST) and Very Large Array (VLA) observations of the OH Megamaser (OHM) galaxy IRAS 11506-3851. The HST images reveal an isolated spiral galaxy and the combination with the GMOS-IFU flux distributions and VLA data allow us to identify a partial ring of star-forming regions surrounding the nucleus with a radius of ≈ 500 pc. While this ring shows starburst excitation and low velocity dispersion, the region internal to the ring shows higher excitation and velocity dispersion values, with values increasing towards its borders at ≈ 240 pc from the nucleus, resembling a projected bubble. The enhanced excitation and velocity dispersion of this bubble surrounds a 8.5 GHz radio emission structure, supporting its origin in a faint AGN that is mostly shocking the surrounding gas via a plasma ejection seen in radio at the present stage. This is the fourth of the 5 OHM galaxies we have studied so far (from our sample of 15 OHM) for which GMOS-IFU data indicate the presence of a previously unknown faint AGN at the nucleus, consistent with the hypothesis that OHM galaxies harbor recently triggered AGN.

Key words: galaxies:active – galaxies:ULIRGs – galaxies:kinematics and dynamics – galaxies:ISM

1 INTRODUCTION

Ultra-Luminous Infrared Galaxies (ULIRGs) are luminous galaxies in the infrared ($L_{IR} \geq 10^{12} L_{\odot}$; Soifer et al 1987), most of which are the result of advanced mergers of galaxies (e.g., Sanders et al 1996), and present large amounts of molecular gas in their nuclear region (inner few kpc). Although vigorous star formation is usually seen in these objects, and certainly contributes to the high luminosity of the nucleus, it is not yet clear if and how much can also be contributed by an embedded Active Galactic Nucleus (AGN). Many studies indeed argue that the most luminous AGN ($L \geq 10^{42} L_{\odot}$) are preferentially hosted by galaxy mergers (Storchi-Bergmann & Schnorr-Müller 2019, and references therein).

Many ULIRGs host OH Maser and Megamaser emis-

sion, which are the result of stimulated emission appearing at the frequencies 1665 and 1667 MHz lines with luminosities $10^2 - 4 L_{\odot}$ (Darling & Giovanelli 2002; Lo 2005). Galaxies presenting such emission are called OH Megamaser (OHM) galaxies. There is evidence that many of these OHM galaxies host an AGN that is still immersed in dense layers of dust and gas, suggesting that they could represent a key stage in galaxy evolution in which the AGN is being triggered by the accretion of matter to the central supermassive black hole (SMBH). (Sanders et al 1988a; Barnes & Hernquist 1992; Hopkins et al 2006; Haan et al 2011).

Theoretical models and numerical simulations attribute a key contribution from Starbursts and AGN feedback to galaxy evolution (Hopkins et al 2012; Nelson et al 2015; Pereira-Santaella et al 2018; Schaye et al 2015). This contribution occurs through the injection of matter and energy into the interstellar medium, originating outflows that play an important role in regulating the growth of the galaxy

* E-mail: hekatelyne.carpes@gmail.com (CH)

stellar mass and the accretion of matter to the central supermassive black hole (SMBH). Such gas outflows are commonly detected in ULIRGS (Arribas et al 2014; Cazzoli et al 2016; Ciccone et al 2014).

This work is part of an ongoing project aimed to investigate the nature of OHM galaxies using Hubble Space Telescope (HST), Very Large Array (VLA) images and Integral Field Spectroscopy (IFS) data. In particular, our goal is to investigate the hypothesis that the megamaser traces a phase in the galaxy in which the AGN is being triggered. We began this study with an initial sample of 15 OHM galaxies selected for being on different merger states – as it is known that the megamaser is also linked to galaxy mergers and star formation – in order to investigate if the presence of the AGN is linked to a specific stage of the merger.

In previous papers we discussed the kinematics and excitation of the gas as well as the radio emission in four OHM galaxies. The main results of these works are summarized as follows. Sales et al (2015) performed a multi-wavelength analysis of the OHM galaxy IRAS 16399-0937, concluding that it harbors an embedded AGN of relatively modest luminosity and that it is also the likely source of the OHM emission observed in this system, while the other nucleus is starburst dominated. In Hekatelyne et al (2018a), we used Gemini Multi-Object Spectrograph (GMOS) integral field unit (IFU), VLA and HST, which reveal an obscured type 2 AGN and its outflow in the OHM galaxy IRAS F23199+0123. We also found knots of star formation in the nuclear region of the eastern galaxy of the pair and report a new OH maser detection. In Hekatelyne et al (2018b) we used multi-wavelength data to conclude that IRAS 03056+2034 presents evidence of an embedded AGN and circumnuclear star formation that also contributes to the ionization of the gas. Finally, in Sales et al (2019), multi-wavelength observations show that IRAS 17526+3253 presents two kinematic components and the emission-line ratio diagnostic diagrams indicate that young stars are the main source of ionization for both of them. Although we find evidence of gas ionized by AGN, the number of objects is still too small to drive a firmer conclusion about the nature of OHM galaxies.

Here we present multi-wavelength observations of another OHM galaxy, IRAS 11506-3851 (hereafter IRAS 11506, also identified as ESO 320-G030), which is an isolated spiral galaxy (Bellocchi et al 2013, 2016) showing a double-barred structure (Greusard et al 2000) with no clear evidence of having suffered a major merger and hosting a weak maser (Norris et al (1986)), what is consistent with results from previous studies that show that major mergers host more powerful OHMs.

The weak maser in IRAS11506 shows two components: a stronger OH feature accompanied by a weaker, and slightly blueshifted one. Each feature has a half-power width of $\approx 120 \text{ km s}^{-1}$, which is typical of OHM. Moreover, considering $H_0 = 75 \text{ km s}^{-1} \text{ Mpc}^{-1}$, they estimated that the isotropic luminosity of the OH emission is $\approx 52 L_\odot$ (Norris et al 1986).

IRAS 11506 is a local (46 Mpc; scale of $240 \text{ pc arcsec}^{-1}$, Cazzoli et al (2014)) LIRG ($\log L_{\text{IR}}/L_\odot = 11.3$) classified as presenting an HII (or Starburst) nucleus from optical spectroscopy (Van der Broek et al 1991). Previous studies reveal a resolved outflow in neutral (Cazzoli et al 2014) and molecular gas using Atacama large Millimetric Array (ALMA) observations (Pereira-Santaella et al 2016).

We use spectroscopic data obtained with the GMOS-IFU, combined with VLA and HST images of IRAS11506 to map the stellar and gas kinematics and distributions, as well as the gas excitation in the inner kpc of the galaxy. This paper is organised as follows: in Section 2 we describe the observations and data reduction. Section 3 presents our results, in Section 4 we discuss the nature of the nuclear source and gas kinematics and we present our conclusions in Section 5.

2 OBSERVATIONS AND DATA REDUCTION

2.1 HST data

HST continuum and emission-line imaging of 15 OHM galaxies were obtained in Program 1160 (PI D. J. Axon), including IRAS 11506. The data were obtained with the Advanced Camera for Surveys (ACS) using wide, broad, narrow and medium-band filters. The reduction process was performed using Image Reduction and Analysis Facility (IRAF) (Tody 1986, 1993) routines and followed the basic procedures described in Sales et al (2019). Figure 1 shows the ACS F814W continuum and narrow-band images in $\text{H } \alpha + [\text{N II}] \lambda\lambda 6548, 84$ emission lines, highlighting the observed structure within the GMOS-IFU field-of-view (hereafter FoV).

2.2 VLA radio continuum data

We reduce 1.43 and 4.86 GHz archival data acquired with the VLA in the A-array configuration and 8.46 GHz data in the AB-array configuration (AL508) using standard calibration and imaging procedures in AIPS. A couple of rounds of phase-only and phase+amplitude self-calibration were carried out interactively using the AIPS task CALIB before producing the final radio images. The *rms* noise in the 1.43 and 4.86 GHz images are 0.1 mJy/beam and 90 mJy/beam, respectively. We create an 1.43 - 4.86 GHz spectral index image using the task COMB after convolving the images at the two frequencies with a circular beam of $2''.5$; flux density values below the 3 sigma level were blanked. Figures 2 and 3 show the radio continuum image at 8.5 GHz and the 1.43-4.86 GHz spectral index image, respectively.

2.3 GMOS-IFU data

IRAS11506 was observed at the Gemini South Telescope GMOS-IFU (Allington-Smith et al. 2002). The observations were carried out on the nights of 2014 April 20, 21 and 2014 May 08,18 splitted into 23 individual exposures, 17 of them having exposure times of 1200 sec and 6 of them of 1100 sec.

The observations were done with the IFU operating in the one-slit mode using the IFU-R mask, with the grating B600_G5323 and the filter GG455_G0329. We obtain spectra centred at three distinct wavelengths (6200\AA , 6300\AA and 6400\AA) to properly correct for the gaps between the detectors and we orient the IFU along position angle 358° , chosen to find suitable guide stars. This configuration corresponds to a FoV of $3''.5 \times 5''.0$, and spectral range is such that it includes the strongest optical lines, from $\text{H}\beta$ to $[\text{S II}] \lambda 6731\text{\AA}$.

The processing of the data was performed using the GEMINI IRAF package following the standard procedures of

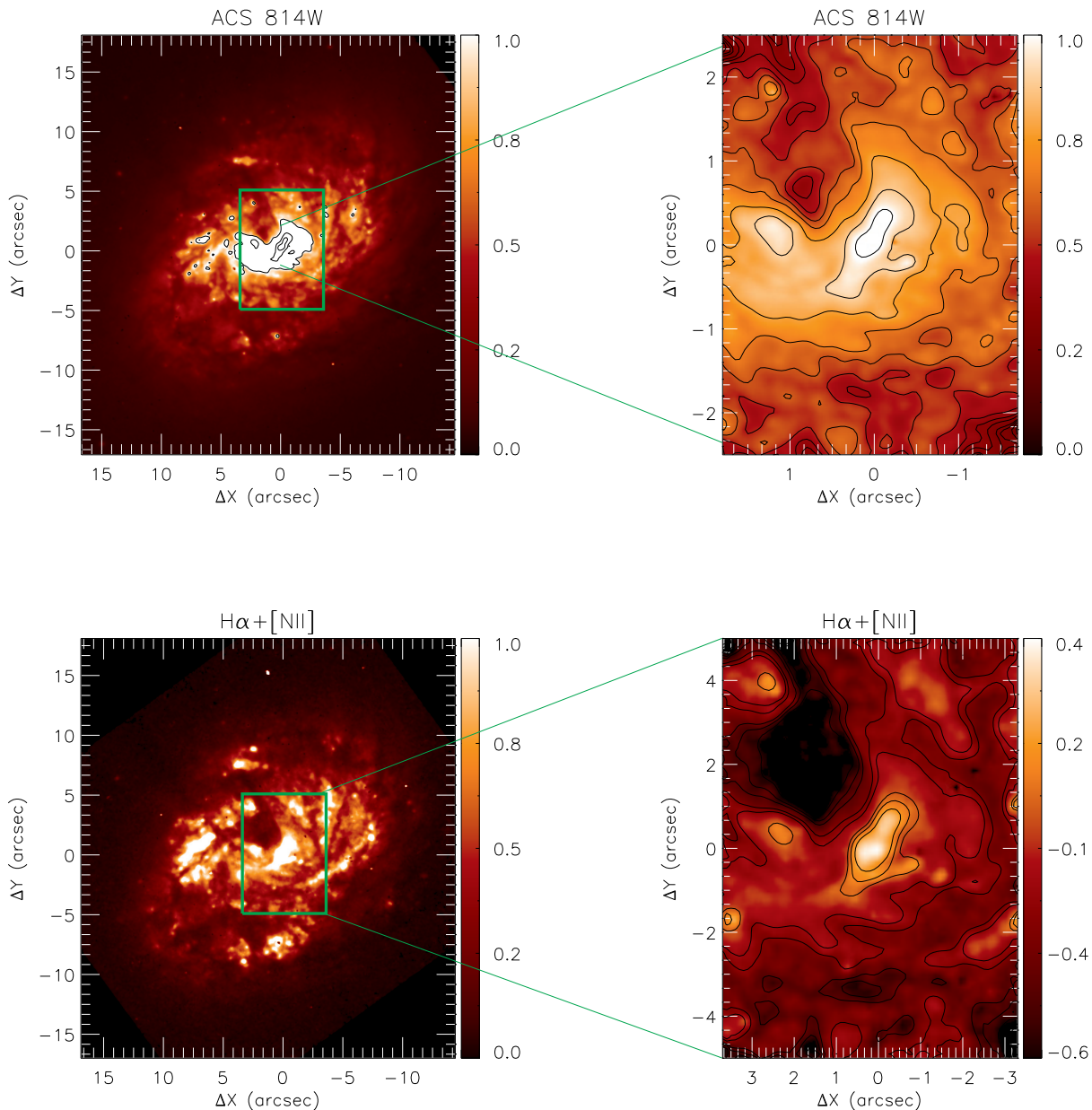


Figure 1. HST images of IRAS 11506. Left panels: Large-scale images, showing in the top panels the ACS/HST F814W - i band images and, in the bottom panels, the $H\alpha + [NII]\lambda\lambda 6548, 84$ narrow-band images. Right panels: zoom-in of the images in the left showing the region observed with GMOS-IFU, whose FoV ($3'' \times 5'' \times 5''$) is shown as the green rectangles. The color bars show the fluxes in arbitrary units.

spectroscopic data reduction. The main steps include the subtraction of the bias level for each image, flat-fielding and trimming. We then perform the wavelength calibration using the spectra of CuAr lamps as reference, followed by the subtraction of the sky emission. The sensitivity function was obtained from the spectrum of the EG 131 standard star in order to flux calibrate the spectra. We finally obtain a data cube for each exposure, which were then median combined using the GEMCOMBINE routine, resulting in a single data cube for the object. During this step we used the peak of the

continuum emission as reference and the SIGCLIP algorithm to remove bad pixels and remaining cosmic-ray contamination.

The seeing during the observation is $\sim 0''.6$, as obtained from the measurement of the full width at the half maximum (FWHM) of the flux distribution of the standard star EG131. This translates to ~ 115 pc at the galaxy considering a distance of 46 Mpc (Cazzoli et al 2014). The velocity resolution is $\sim 80 \text{ km s}^{-1}$, as estimated from the measurement

of the FWHM of typical emission lines of the CuAr lamps spectra.

3 RESULTS

3.1 HST images

In Figure 1, we present in the ACS/HST F814W i-band image (top panel) and the narrow-band $H\alpha + [N II]\lambda\lambda 6548, 84$ image (bottom panel) of IRAS11506. The panels on the left-hand show large scale images of the galaxy and the green boxes represent the FoV of the GMOS-IFU data. The right-hand panels present zoomed images of the galaxy within the same FoV of the GMOS-IFU data.

The i-band image reveals the spiral structure of the galaxy with the highest fluxes observed at its nucleus. The zoomed i-band image shows a region of fainter emission to the north-east of the nucleus, possibly due to a higher dust extinction in that region. In addition, several knots of emission are seen surrounding the nucleus, with the brightest structure resembling a partial ring or segments of spiral arms.

The continuum-free HST $H\alpha + [N II]\lambda\lambda 6548, 84$ narrow-band image presents a flux distribution similar to that of the i-band image, with the strongest emission along $PA \approx 135/345^\circ$ and several knots of emission associated to regions with the enhanced i-band continuum fluxes.

3.2 VLA images

Figure 2 presents the VLA continuum image at 8.5 GHz that reveals a two-sided core-jet-like structure in the east-west direction of extent $5''.5$. This extension is better defined in the 1.4-4.9 GHz spectral index image which shows a steep spectral shape (spectral index of -0.80 ± 0.11) along the same direction. The core spectral index is relatively flatter at -0.54 ± 0.01 .

An elongation is clearly seen in the 1.4-4.9 GHz spectral index map of Figure 3 actually more along the southeast-northwest direction (instead of east-west direction), while the highest spectral index values of -0.5 are found at the nucleus.

3.3 GMOS-IFU Emission-line flux distributions

We have mapped the emission-line flux distributions of $H\alpha$, $H\beta$, $[O III]\lambda 5007$, $[O I]\lambda 6300$, $[N II]\lambda 6584$ and $[S II]\lambda 6731$ (hereafter $[O III]$, $[O I]$, $[N II]$ and $[S II]$, respectively) lines by fitting the line profiles by Gaussian curves. The fitting is done using a modified version of the PROFIT routine (Riffel 2010), adopting a similar fitting procedure as described in Freitas et al (2018). In short, each line is fitted by a single Gaussian component and the underlying continuum is represented by a linear equation fitted to continuum regions, next to each line profile. We fit the $H\beta + [O III]$ line complex simultaneously, tying the width and velocity of the $[O III]\lambda 4959$ and $[O III]\lambda 5007$ emission lines and keep fixed their flux ratio to the theoretical value of $[O III]\lambda 5007/[O III]\lambda 4959 = 3$ (Osterbrock 1989). A similar procedure is adopted for the $H\alpha + [N II]$ complex, where we tie the kinematics of the $[N II]$

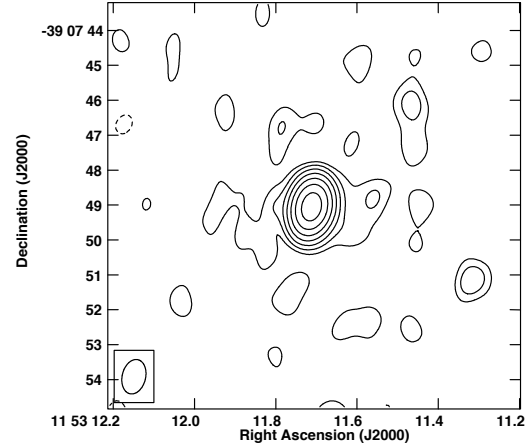


Figure 2. VLA radio continuum images at 8.5 GHz. The peak surface brightness and lowest contour level is 25.9 mJy/beam and $\pm 1\%$, respectively. The beam is 1.00×0.67 arcsec at a $PA = -13.5$ degrees.

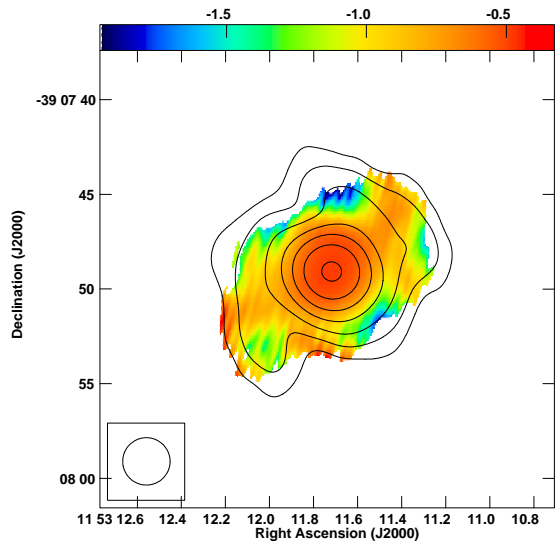


Figure 3. Radio spectral index image of IRAS11506, derived from 1.4 and 4.9 GHz VLA images at a resolution of 2.5 arcsec. The contours are at 1.4 GHz with the lowest contour level and peak surface brightness value being $\pm 1.4\%$ and $5.8E-2$ Jy/beam.

lines and $[N II]\lambda 6583/[N II]\lambda 6548 = 3$. The kinematics of the $[S II]$ lines is also tied, while the $[O I]$ is fitted separately.

Figure 4 shows three representative spectra of different regions probed by our observations: the nucleus (N in Fig. 5), a region between the nucleus and the ring of star forming regions (A in Fig. 5) and a region in the ring (E in Fig. 5).

Figure 5 shows the $H\beta$, $[O III]$ and $[O I]$ flux maps in the

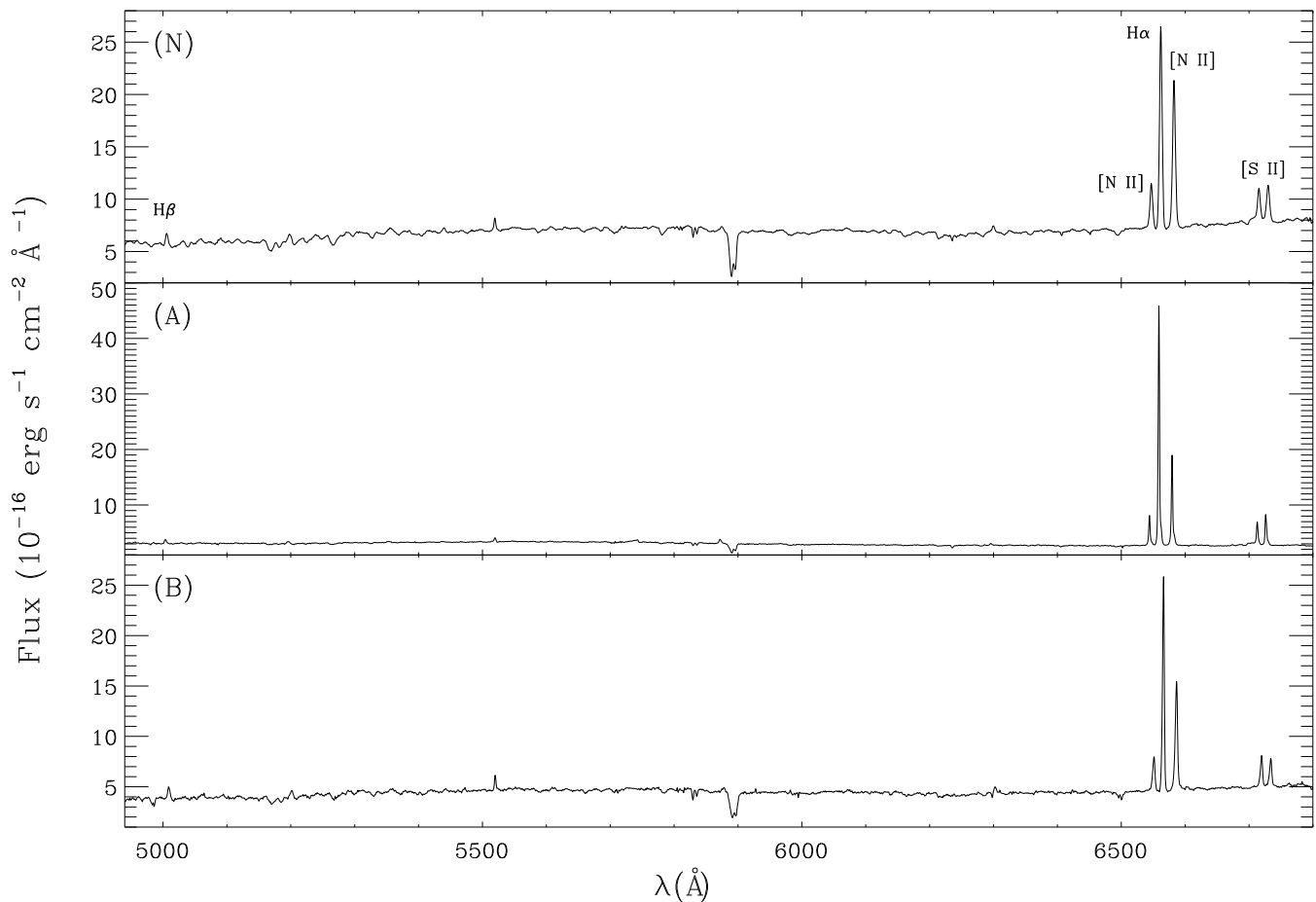


Figure 4. Three representative spectra of the different regions probed by our observations, from top to bottom: the nucleus (N in Fig.5), a region between the nucleus and the ring (A in Fig.5) and a region in the ring (E in Fig.5)

top panels and for the $H\alpha$, $[N II]$ and $[S II]$ in the bottom panels. The central cross in all maps indicates the position of the nucleus (identified with the peak of continuum emission) and grey regions represent masked locations where the signal-to-noise ratio was not high enough to allow reliable measurements of the emission lines or locations with no detection of line emission. These locations present flux uncertainty larger than 30 per cent. The color bars show the fluxes in logarithmic units of $\text{erg s}^{-1} \text{cm}^{-2} \text{spaxel}^{-1}$.

The $H\alpha$ and $H\beta$ emission-line maps reveal the strongest emission at $\sim 2''.0$ north-northwest from the nucleus, in regions identified as E and F in the $H\alpha$ map of Fig. 5. These regions are part of a partial ring of knots of enhanced emission seen at $\approx 2''$ (≈ 500 pc) from the nucleus, which may be due to circumnuclear star-forming regions (CNSFRs). For simplicity, we will call this structure hereafter, as the “ring”. The nucleus shows a somewhat lower emission, as compared to the CNSFRs and the lowest emission is seen to the north-east of the nucleus.

In the $[N II]$ and $[S II]$ flux maps the nucleus is somewhat more luminous than the brightest CNSFRs of the ring (regions E and F), while in the $[O III]$ and $[O I]$ maps the nucleus is much more luminous than the ring, indicating a distinct nature for the gas excitation of the nucleus and the ring. In the case of the $[O III]$ flux map, the nuclear emission is the

most extended among all lines, and delineates an elongated structure of $\approx 1.5''$ (360 pc) running from the south-east to the north-west. Another region of enhanced $[O III]$ emission is observed at $\approx 1''.3$ (270 pc) east to south-east of the nucleus, which is not seen in the other emission-line maps.

3.4 Emission-line ratio maps

From the emission-line flux distributions, we obtained the reddening and electron density N_e distributions, shown in Figure 6 together with the line ratio maps $[O III]/H\beta$, $[N II]/H\alpha$, $[O I]/H\alpha$ and $[S II]\lambda\lambda 6717, 6731/H\alpha$.

The color excess map $[E(B - V)]$ is obtained from the $H\alpha/H\beta$ flux ratio following the procedure described in Freitas et al (2018). The values of $E(B - V)$ range from 0.1 to 0.5, with the highest ones observed to the south-west of the nucleus.

The ionised gas density map N_e was obtained from the $[S II]\lambda 6717/6731$ line ratio assuming an electronic temperature $T_e = 10,000$ K using the *temden* IRAF routine. The map shows values ranging from 100 to 500 cm^{-3} with the highest ones observed to the south and south-west of the nucleus and at the borders of the FoV.

The $[O III]/H\beta$ ratio map shows the lowest values (≤ 0.1) at the ring and the highest values (of up to 0.6) in a knot

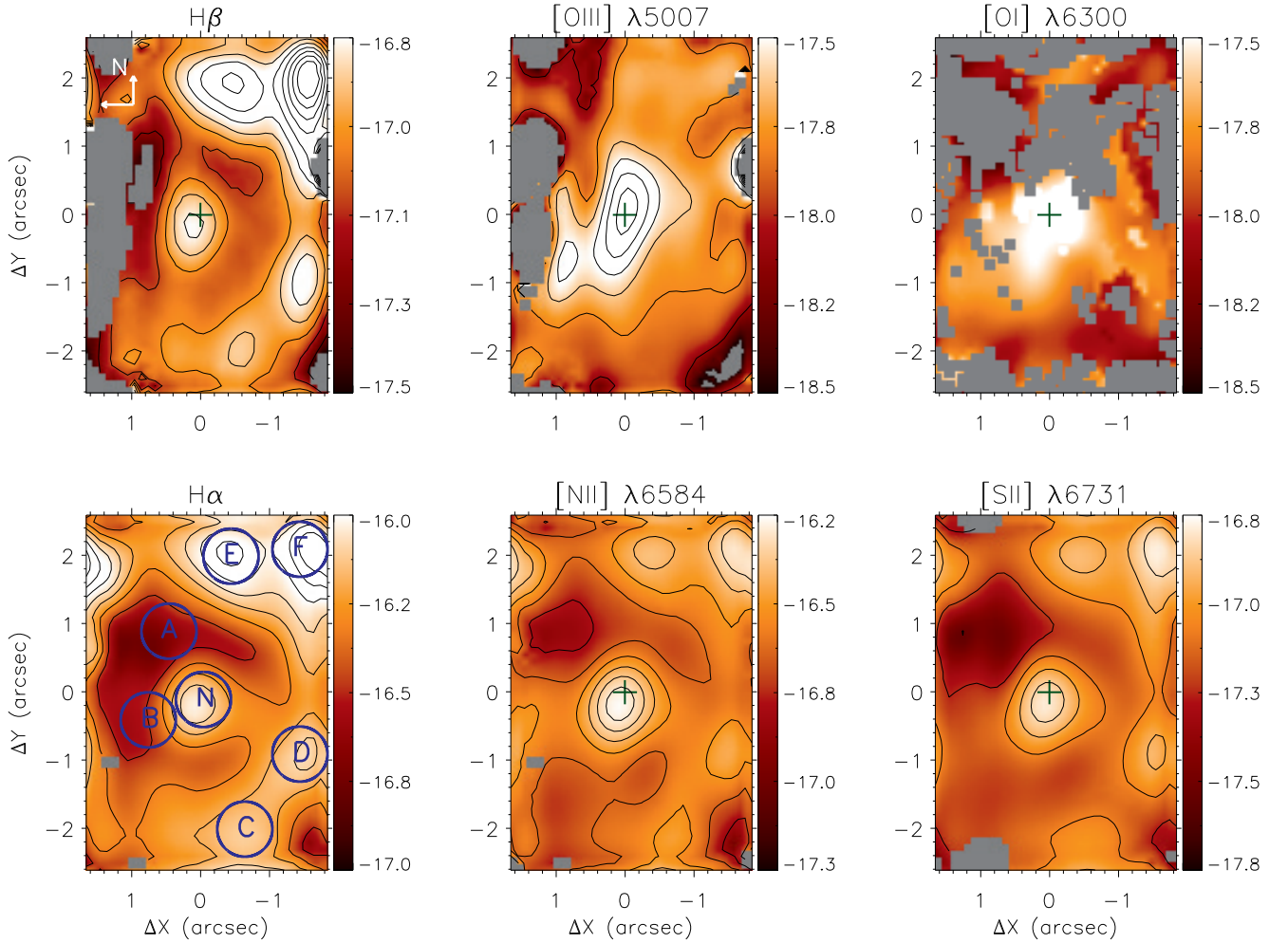


Figure 5. Top panels: flux maps for $H\beta$ (left), $[O\text{ III}]\lambda 5007$ (centre) and $[O\text{ I}]\lambda 6300$ (right) emission-lines of IRAS11506. Bottom panels: flux maps for $H\alpha$ (left), $[N\text{ II}]\lambda 6584$ (centre) and $[S\text{ II}]\lambda 6731$ (right). The central crosses in all maps mark the position of the nucleus and grey regions represent masked locations, where the signal-to-noise ratio was not high enough to obtain reliable fits of the emission-line profiles or locations with no line detection. The blue circles in the $H\alpha$ flux map delimit the regions where we have extracted spectrum to characterize the star-forming properties (see Fig. 4). The color bars show the fluxes in logarithmic units of $\text{erg s}^{-1}\text{cm}^{-2}\text{spaxel}^{-1}$.

extending to $1''$ (240 pc) north-west of the nucleus and in an elongated region at $1''.3$ (312 pc) east and south-east of it, which together with the surrounding values inside the ring show a structure that seems to delineate the borders of a ≈ 500 pc diameter bubble somewhat off-centered relative to the nucleus.

The $[N\text{ II}]/H\alpha$ and $[S\text{ II}]/H\alpha$ maps show the highest values at locations where the $[O\text{ III}]/H\beta$ and $[N\text{ II}]/H\alpha$ are also higher than in the surroundings, better defining the off-centered bubble described above. Although more noisy, the $[O\text{ I}]/H\alpha$ ratio map also shows this bubble.

3.5 Stellar kinematics

We use the penalized Pixel-Fitting pPXF routine (Cappellari & Emsellem 2004; Cappellari 2017) for fitting the absorption spectra of IRAS11506 and measure the stellar kinematics. To perform the measurements we use as spectral templates, the Single Stellar Populations (SSP) models of

Bruzual & Charlot (2003), which have similar spectral resolution of the GMOS data and have been previously used to measure the stellar kinematics of nearby galaxies from GMOS-IFU data (Brum et al. 2017). The line-of-sight velocity distribution of the stars is assumed to be Gaussian, as we fit only the two first moments (V_* and σ_*). We fit the spectral range from 5050 to 6100 Å, masking out emission lines and regions where no absorption lines are present, allowing the use of multiplicative polynomials of order 4 to correct the shape of the continuum and we use the *clean* parameter to reject all spectral pixels deviating more than 3σ from the best fit, to exclude possible remaining spurious features.

The pPXF routine provides as output the measurements of the stellar velocity V_* and velocity dispersion σ_* as well as their corresponding uncertainties. Figure 7 shows the corresponding two-dimensional maps. Locations in white in the velocity field and in gray in the velocity dispersion map are masked locations, corresponding to spaxels where the un-

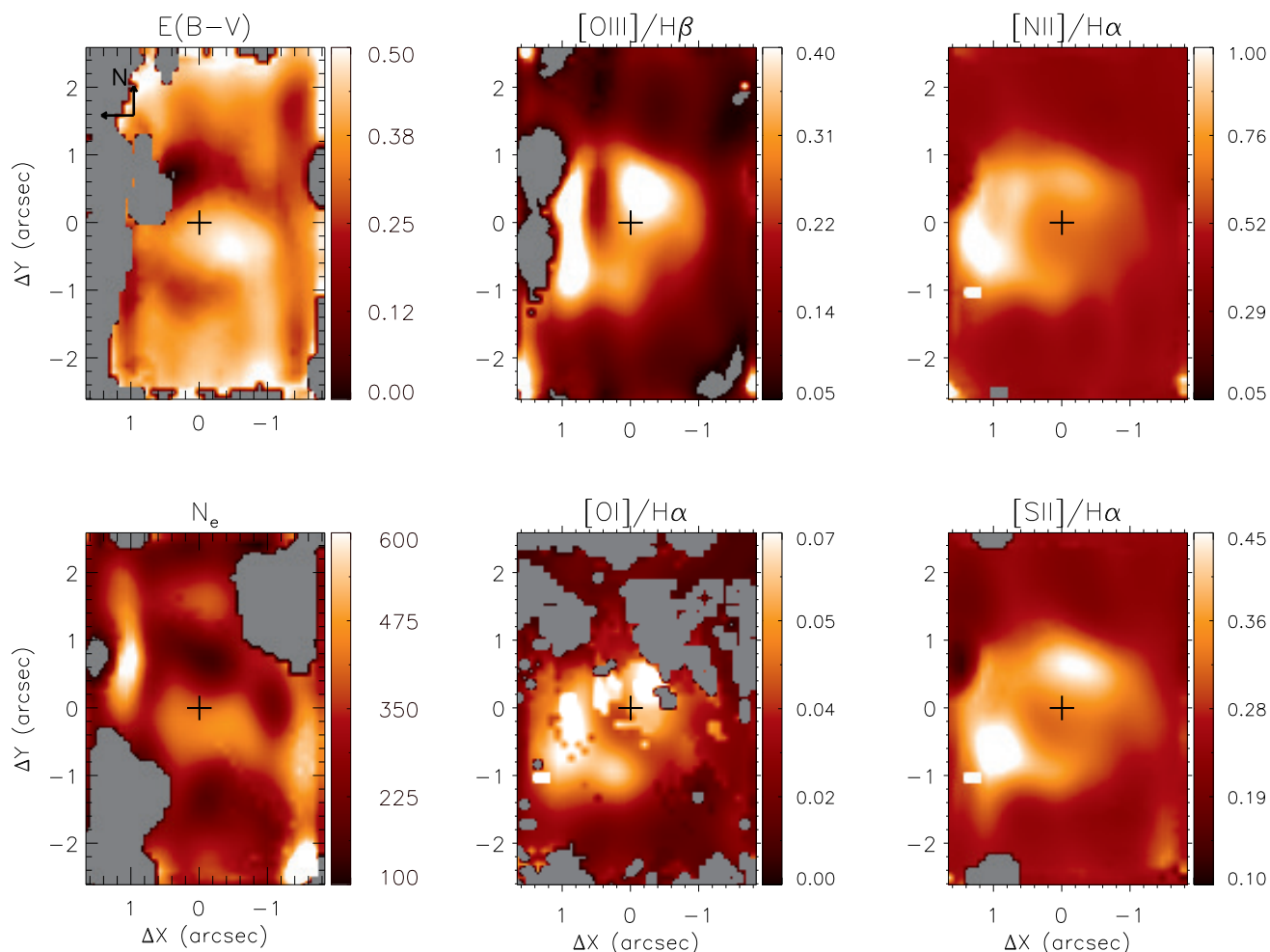


Figure 6. Top panels: $E(B-V)$ map obtained from the $H\alpha/H\beta$ line ratio (left), emission-line ratios of $[O\text{ III}]/H\beta$ (centre) and $[N\text{ II}]/H\alpha$ (right). Bottom panels: Electron density map for IRAS11506 obtained from the $[S\text{ II}]$ emission-lines, which the colour bar shows the N_e values in units of cm^{-3} (left), emission-line ratios of $[O\text{ I}]/H\alpha$ (centre) and $[S\text{ II}]/H\alpha$ (right).

certainties in V_* and/or σ_* are larger than 30 km s^{-1} . The systemic velocity of the galaxy (3076 km s^{-1}), corrected for the heliocentric rest frame is subtracted from the observed velocity, as obtained from the fitting of the rotation disk model discussed in Sec. 4.2. The stellar velocity field shows a well defined rotation pattern with blueshifts to the north-west and redshifts to the south-east with a projected velocity amplitude of about 120 km s^{-1} .

The stellar velocity dispersion map presents the larger values (of $\approx 140\text{ km s}^{-1}$) along $PA \approx 135/315^\circ$, coincident with the orientation of the elongated structure seen in the HST continuum image (Fig. 1). The smallest values of $70\text{--}100\text{ km s}^{-1}$ are observed mainly to the southwest of the nucleus.

3.6 Gas Kinematics

Figure 8 shows the line-of-sight velocity and velocity dispersion maps for $[O\text{ III}]$, $H\alpha$ and $[N\text{ II}]$ emission lines. As for the stellar velocity field, the velocities are shown relative to the systemic velocity of the galaxy estimated in Sec. 4.2.

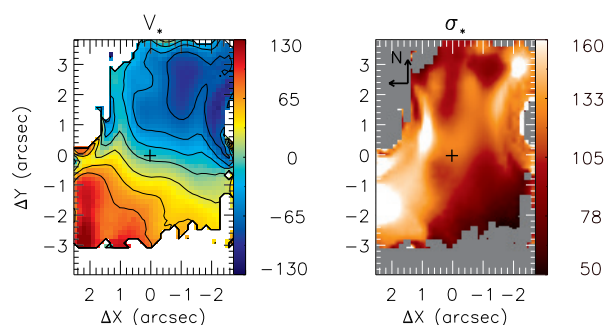


Figure 7. Stellar centroid velocity field and stellar velocity dispersion for IRAS11506. The color bars are in units of km s^{-1} . The central crosses mark the location of the nucleus.

The velocity fields of all the emission-lines are very similar and present a disturbed rotation pattern with blueshifts and redshifts observed to the north-west and south-east of the nucleus, respectively, similar to that of the stellar velocity

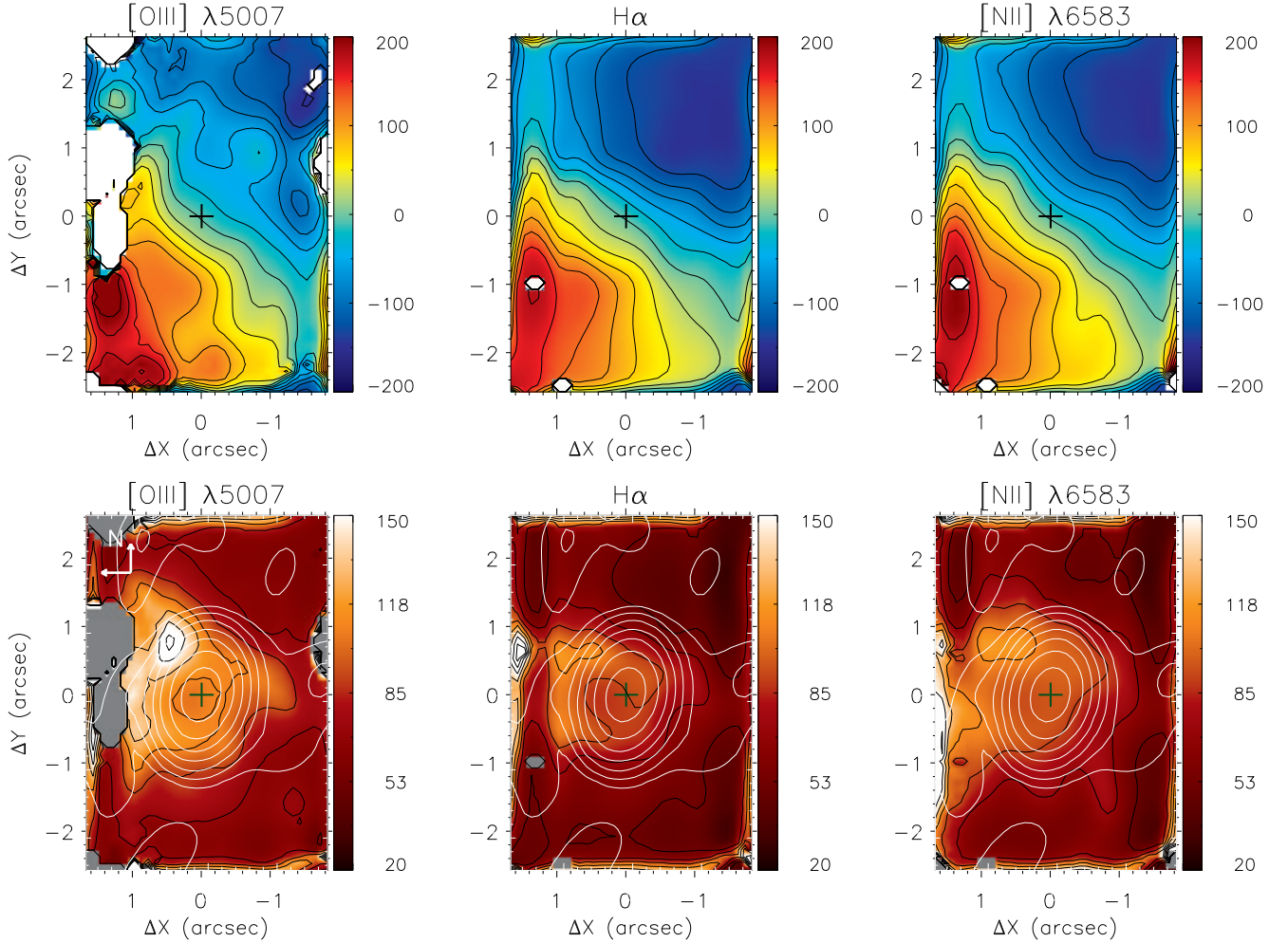


Figure 8. Top panels: line-of-sight velocity fields for the [O III] (left), H α (centre) and [N II] (right) emitting gas. The color bars show the velocities in units of km s^{-1} , after the subtraction of the systemic velocity of the galaxy. Bottom panels: velocity dispersion maps for the [O III] (left), H α (centre) and [N II] (right) emission-lines, corrected for the instrumental broadening. The white contours presented in the residual map are at 8.5 GHz. The color bars show the σ values in units of km s^{-1} . The central cross in all panels marks the position of the nucleus

field. The velocity amplitude is nevertheless larger than that of the stellar velocity field, reaching about 200 km s^{-1} .

The velocity fields are distorted when compared to a rotation velocity field, and, in the case of H α and [N II], the blueshifted side shows a steeper gradient than the redshifted side, while for the [O III] the two gradients are more similar, but the velocity field is noisier.

The bottom panels of Figure 8 show the velocity dispersion maps, with values ranging from ≈ 40 to 150 km s^{-1} for all emission lines. The highest values are observed for the [O III] $\lambda 5007$ in the “triangular-shaped” or ring-shaped region where the highest emission-line ratios are also observed, as discussed in Section 3.4. This region is also co-spatial with the location of the strongest radio emission, as evidenced by the radio contours from Fig. 2 overplotted on the velocity dispersion maps.

4 DISCUSSION

4.1 Gas excitation

4.1.1 Star-forming regions properties

Fig. 5 shows knots of strong emission in H α , H β , [N II] and [S II], also seen (although with much better angular resolution) in the H α + [N II] HST images of Fig. 1, forming a partial ring with on-going star formation. We extract spectra at the location of the emission-line knots along the ring, labelled as C, D, E and F in Fig. 5 plus one from the nucleus (N) and another two (A and B) between the nucleus and the ring. These spectra were obtained by integrating the fluxes within circular apertures of $0''.4$ radius. We derive the following properties: the H α luminosity, the ionized gas mass, the number of ionizing photons and the star formation rates at the corresponding locations. These properties are listed in table 1.

We first measure the H α fluxes to derive the luminosity

Table 1. Physical properties of the star-forming regions in IRAS11506.

Region	$L_{H\alpha}$ (10^{39} erg s $^{-1}$)	M ($10^4 M_{\odot}$)	log Q[H $^{+}$] (s $^{-1}$)	SFR ($10^{-3} M_{\odot}$ yr $^{-1}$)
N	6	1.5	50.79	5
A	2	0.5	50.31	2
B	2	0.6	50.41	2
C	6	0.9	50.79	5
D	6	0.9	50.79	5
E	10	2.5	51.01	8
F	9	2.3	50.96	7

of the knots. To obtain the mass of ionized gas we used the following expression from [Peterson \(1997\)](#):

$$\frac{M}{M_{\odot}} \approx 2.3 \times 10^5 \frac{L_{41}(H_{\alpha})}{n_3}, \quad (1)$$

where L_{41} is the $H\alpha$ luminosity in units of 10^{41} erg s $^{-1}$ and n_3 is the electron density in units of 10^3 cm $^{-3}$. We assume $N_e=300$ cm $^{-3}$, which is the mean value of the electron density of the CNSFRs estimated from the [S II] λ 6717/ λ 6731 intensity ratio (see also Fig. 6). We find values for the mass of ionized gas for each CNSFR ranging from $5 \times 10^3 M_{\odot}$ to $2.5 \times 10^4 M_{\odot}$.

In order to obtain the rate of ionizing photons Q[H $^{+}$] for each star-forming region we used the following relation by [Osterbrock \(1989\)](#) and the procedure described in [Hekatelyne et al \(2018a\)](#):

$$\left(\frac{Q[H^{+}]}{s^{-1}} \right) = 1.03 \times 10^{12} \left(\frac{L_{H\alpha}}{s^{-1}} \right). \quad (2)$$

The Star Formation Rate (SFR) was derived under the assumption of continuous star formation regime, using the relation ([Kennicutt 1998](#)):

$$\frac{SFR}{M_{\odot} \text{ yr}^{-1}} = 7.9 \times 10^{-42} \frac{L_{H\alpha}}{\text{erg s}^{-1}}. \quad (3)$$

We obtain values of the ionizing photons rate (log Q[H $^{+}$]) ranging from 50.31 to 51.01 and values of SFRs in the range 2 to 8 ($10^{-3} M_{\odot}$ yr $^{-1}$). The ionizing photons rate values are in agreement with other measurements obtained for nearby Seyfert galaxies (e.g. [Wold & Galliano 2006](#); [Galliano & Alloin 2008](#); [Riffel et al. 2009, 2016](#); [Hennig et al. 2018](#); [Hekatelyne et al 2018a,b](#)).

4.1.2 Diagnostic diagrams

We use the emission-line ratios from the GMOS-IFU data to investigate the nature of the gas emission via the BPT diagnostic diagrams proposed by [Baldwin, Phillips & Terlevich \(1981\)](#). These diagrams allow us to distinguish the gas excitation over the GMOS FoV as characteristic of Starburst, AGN or composite (hereafter used to identify a region with composite Starburst and AGN excitation).

We present three diagnostic diagrams and an excitation map presented in Figure 9, where each spaxel within the FoV corresponds to a point in these diagrams. The dashed curve is from [Kauffmann et al. \(2003\)](#) and the dotted one from [Kewley et al. \(2001\)](#) which have been used to distinguish ionization due to Starburst, AGN and composite.

The top panels of Fig. 9 show the [O III]/H β versus

[O I]/H α and the [O III]/H β versus [S II]/H α diagrams. Almost all spaxels are to the left of the Kewley’s line, indicating that the gas excitation is dominated by Starburst activity and just a few spaxels show excitation that could be due to an AGN. The bottom panels of Fig. 9 show the [O III]/H β versus [N II]/H α diagnostic diagram in the left and the corresponding excitation map in the right panel. The [O III]/H β versus [N II]/H α diagnostic diagram shows points both in the region to the left of the Kauffmann’s curve indicating Starburst excitation and in the region between Kauffmann’s and Kewley’s lines, indicating a composite origin for the observed gas emission. We split the composite region in “sub-regions”, one with higher excitation (identified by the dark red points) and another with lower excitation (in light green).

The capital letters N, A, B, C, D, E and F in the [O III]/H β versus [N II]/H α diagram show the location of the regions identified in Fig. 5. While the regions N, A and B are observed in the region that represents composite ionization/excitation the C, D, E and F regions from the ring are observed in the Starburst region, in agreement with the interpretation that they are star-forming regions.

The bottom right panel of Fig. 9 shows that the excitation within the bubble of ≈ 240 pc radius is higher than the starburst excitation of the 500 pc ring, favoring the presence of mixed AGN and starburst excitation in the former region. But we note that the highest excitation is observed not at the nucleus but in regions at ≈ 200 pc from it to the SE, E and NW of the nucleus, at the “borders” of the central bubble. This suggests that shocks are probably responsible to this higher excitation, as supported also by the enhanced gas velocity dispersion in these regions, and discussed further in the next section.

We have checked if shock model sequences, such as those of [Allen et al. \(2008\)](#) that have been successfully used to reproduce similarly enhanced [N II]/H α and [S II]/H α line-ratio values in another OHM galaxy of our sample – IRAS 17526+3253, in [Sales et al \(2019\)](#), could reproduce the above line ratios in IRAS 11506. We concluded that, although the sequence of these line ratios can indeed be reproduced by these shock models, for velocities in the range 100–300 km s $^{-1}$, the [O III]/H β ratio values of IRAS 11506 are too low to be reproduced by such models. Our conclusion is that – although it is clear that shocks are present, they are not the main excitation mechanism of the gas, that seems to be dominated by Starburst excitation, according to the BPT diagrams.

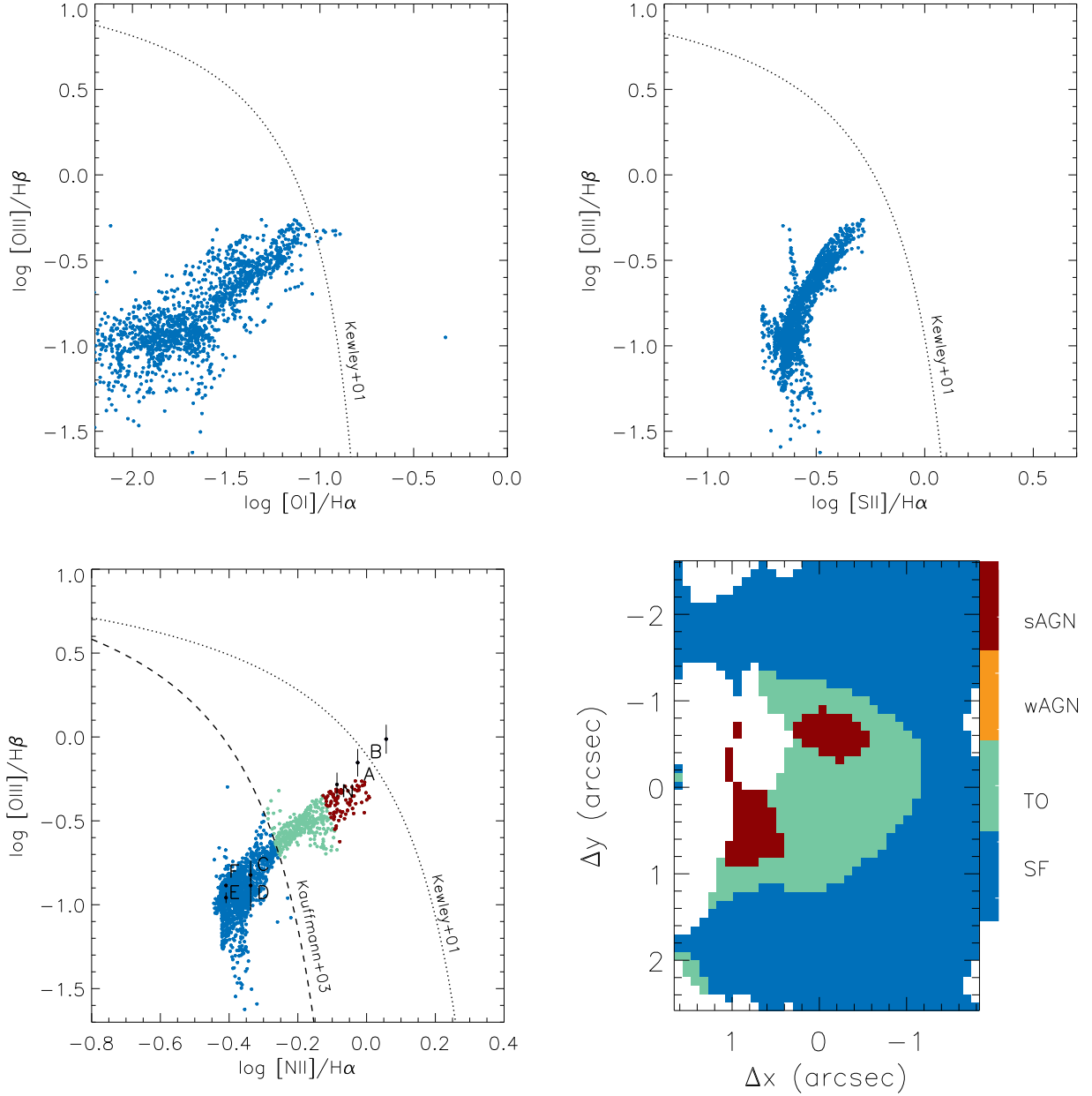


Figure 9. Top panels: $[\text{O III}]\lambda 5007/\text{H}\beta$ versus $[\text{O I}]\lambda 5007/\text{H}\alpha$ diagnostic diagram of IRAS11506 (left). $[\text{O III}]\lambda 5007/\text{H}\beta$ versus $[\text{S II}]/\text{H}\alpha$ diagnostic diagram (right). Bottom panels: $[\text{O III}]\lambda 5007/\text{H}\beta$ versus $[\text{N II}]/\text{H}\alpha$ diagnostic diagram (left). The dotted and dashed lines represent the Kewley and Kauffmann criteria respectively. Excitation map identifying the regions within the FoV presents distinct excitation mechanisms: strong AGN (sAGN), weak AGN (wAGN), Transition object (TO) and star-forming (SF) (right).

4.2 Gas and stellar kinematics

In an effort to understand the stellar and gas kinematics of IRAS11506 we fit the corresponding velocity fields with a rotating disc model. We use an analytical model under the assumption that the stars and gas have circular orbits in the plane of the galaxy (van der Kruit & Allen 1978; Bertola et al. 1991), and that the circular velocity is given by

$$V_{\text{mod}}(R, \psi) = v_s +$$

$$\frac{AR \cos(\psi - \psi_0) \sin(i) \cos^p(i)}{\{R^2 [\sin^2(\psi - \psi_0) + \cos^2(i) \cos^2(\psi - \psi_0)] + c_0^2 \cos^2(i)\}^{\frac{p}{2}}}, \quad (4)$$

where R is the radial distance from the nucleus projected on the plane of the sky and ψ is its corresponding position angle. The systemic velocity of the galaxy is given by v_s , A is the velocity amplitude, ψ_0 is the position angle of the line of nodes, c_0 is a concentration parameter, defined as the radius where the rotation curve reaches 70% of the velocity amplitude and i is the disc inclination relative to

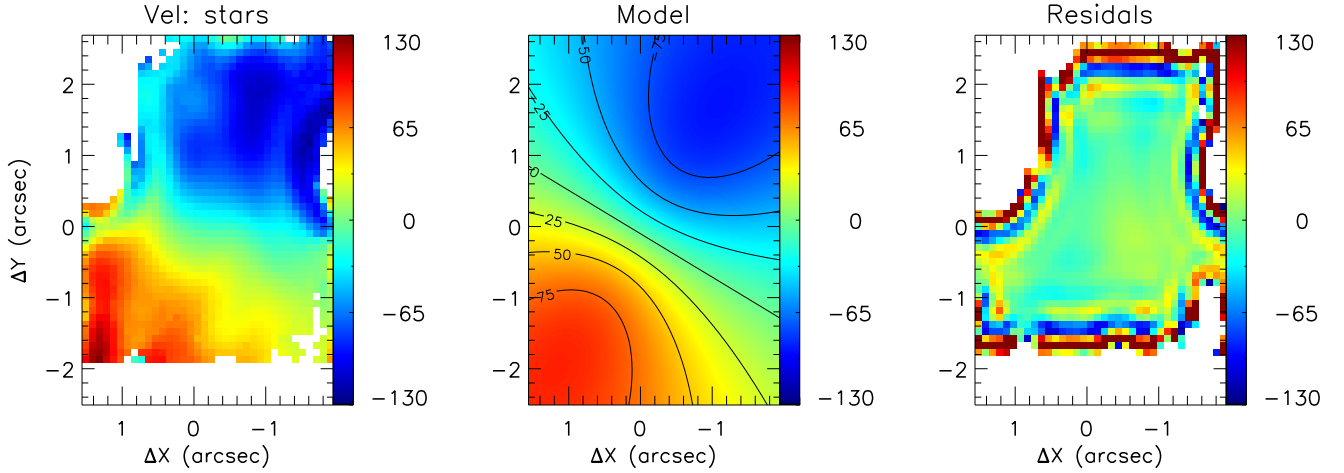


Figure 10. Observed H α stellar velocity field (left), rotating disc model (centre) and residual map (right), obtained as the difference between the observed velocities and the model.

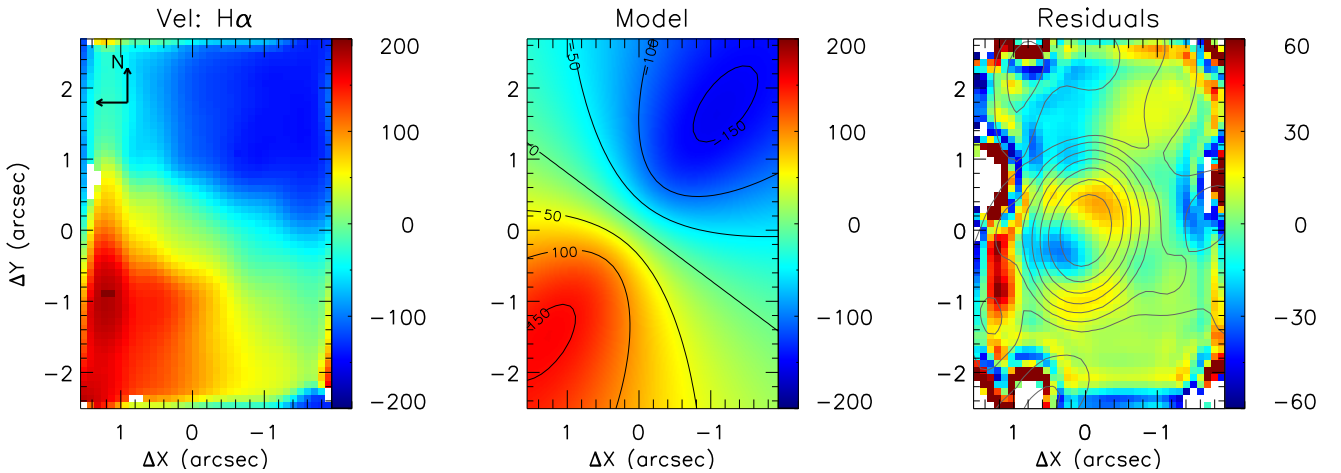


Figure 11. Observed H α velocity field (left), rotating disc model (centre) and residual map (right), obtained as the difference between the observed velocities and the model. The contours presented in the residual map are at 8.5 GHz. The central cross marks the position of the nucleus

the plane of the sky. The p parameter measures the slope of the rotation curve beyond the maximum amplitude, where, usually $1 \leq p \leq \frac{3}{2}$. For $p=1$, the rotation curve at large radius is asymptotically flat while for $p=\frac{3}{2}$ the system has a finite mass.

We fit the stellar and gas velocity fields by the equation above using the MPFITFUN IDL routine (Markwardt et al. 2009) that performs a non-linear least-squares fit. During the fit we fixed the kinematic centre to the position of the continuum peak and the p parameter to $p=1.5$, as we are probing the inner region of the galaxy. The H α velocity field was chosen to represent the gas kinematics because H α is the brightest emission-line over most of the FoV, being also similar to the velocity fields of the other emission lines.

Figure 10 shows the observed stellar velocity field (left), best fit rotation disc model (centre) and the residual map (right) obtained as the difference between the first and the

latter. The velocity residuals are small at all locations (except at the borders of the regions where the uncertainties in the measured velocities are high), indicating that the stellar velocity field is well reproduced by a rotating disc. The resulting parameters for the best fitted model are: $v_s = 3076 \pm 5 \text{ km s}^{-1}$, $A = 283 \pm 14 \text{ km s}^{-1}$, $c_0 = 1''.6 \pm 0''.1$, $\psi_0 = 148^\circ \pm 3^\circ$ and $i = 41^\circ \pm 5^\circ$. Pereira-Santaella et al (2016) used a similar kinematic model to fit the velocity field obtained from the first moment of the CO(2-1) emission. They obtained $v_s = 3080 \pm 4 \text{ km s}^{-1}$, $\psi_0 = 133^\circ \pm 2^\circ$ and $i = 43^\circ$ and so our results are in good agreement with theirs.

Figure 11 presents the observed H α velocity field (left), the rotating disc model (centre) and residual map (right) between these two.

Neglecting the regions of high residuals at the borders of the FoV, which are more affected by noise, the residual

map shows some structures that suggest the presence of non-circular motions. In particular, within $\approx 1''$ from the nucleus, there are residual redshifts to the north-west, with velocities of $\approx 30 \text{ km s}^{-1}$ and residual blueshifts to the opposite direction, south-east, with similar velocities. The resulting parameters for the best fitted model are: $v_s = 3075 \pm 1 \text{ km s}^{-1}$, $A = 365 \pm 6 \text{ km s}^{-1}$, $c_0 = 1''.4 \pm 0''.4$, $\psi_0 = 125^\circ \pm 3^\circ$ and $i = 54^\circ \pm 5^\circ$.

We note that the excess blueshifts and redshifts close to the nucleus along PA= $-45/130^\circ$ are oriented in the direction of spots of increased line ratios of [O III]/H β and [S II]/H α in Fig. 6, coinciding also with the orientation of the elongation seen in the outer contours of the spectral index radio image of Fig. 3. In addition, the radio spectral index image shows approximately constant values in this elongated structure. All these features suggest the presence of a weak bipolar outflow at PA= $-45/130^\circ$.

The gas velocity dispersion maps of Fig. 8 also show increased values along the above PA, but are higher than the surroundings within the whole inner bubble, with the highest values also observed towards the borders of the 240 pc bubble and in particular towards its eastern border, where the [O III]/H β ratio is also highest. The whole region of increased velocity dispersion coincides with the region of strongest radio emission.

We conclude that, although the velocity residuals suggest a modest outflow along PA= $-45/130^\circ$, the most robust signature of feedback from the AGN are the enhanced velocity dispersions towards the borders of the inner bubble suggesting interaction between the plasma bubble and the surrounding medium, pushing and shocking it and producing higher line ratio values.

4.3 The nature of the nuclear emission: is IRAS11506 hiding an AGN?

As discussed in Sec. 4.1.2, we find enhanced gas excitation within the inner 240 pc bubble of IRAS 11506, suggesting the presence of a weak AGN ionizing/exciting the gas there, mixed with Starburst ionization/excitation.

The presence of an additional source of excitation besides the young stars of a Starburst is also supported by the presence of radio emission in the region as revealed by the radio contours in Fig. 8, and the enhanced gas velocity dispersion towards the borders of the bubble where the excitation is also highest. The enhanced velocity dispersion supports the presence of shock excitation, as discussed in the previous section, most probably due to the interaction of the radio bubble with the ambient gas.

The VLA data radio core spectral index is compatible with an AGN (e.g. Sadler et al 1995; Roy et al 2000; Orienti & Pietro 2010; Kharb et al. 2010; Bontempi et al 2012). This implies optically-thin synchrotron emission that could nevertheless also originate in a nuclear starburst. The elongation seen in the spectral index map (Fig. 3), on the other hand, makes the radio core in IRAS11506 to resemble more an AGN radio jet than a nuclear starburst.

The discussion above on the excitation and radio emission suggests that the gas in the inner 240 pc (the inner bubble) is mostly ionised by starbursts in the region. The enhanced velocity dispersion associated with a plasma bubble withing the inner 240 pc and a possible bipolar outflow

supports also the presence of a weak AGN there. We are probably witnessing the birth of an AGN that just emitted a bubble of plasma that is beginning to interact with the surrounding gas via mostly shocks at the present stage.

4.4 Comparison with previous studies

We now compare our results for IRAS 11506 with those recently obtained by previous authors and also with the results of our previous similar studies of OHM galaxies. We have been performing a multiwavelength investigation of the excitation mechanism of these galaxies with the goal of relating the merger state and OH maser properties to Starburst and AGN activity.

4.4.1 Recent results from the literature

Cazzoli et al (2014) studied the multi-phase component structure and wind properties of IRAS 11506 based on IFS obtained with the instruments VIMOS and SINFONI of the Very Large Telescopes (VLT). Their data provide information about kinematic and dynamical properties of the stellar component and gas phases using as tracers the NaD absorption doublet, H α , and the CO bands in the near-infrared. The stellar kinematics they derive from the CO bands is similar to the gas kinematics they derive from H α , showing also a larger rotation amplitude for the gas ($203 \pm 4 \text{ km s}^{-1}$) than for the stars ($188 \pm 11 \text{ km s}^{-1}$).

However, the resolution of the maps of Cazzoli et al (2014) based on the optical data is about 1 arcsec, and, although their Fig. 5 shows an increase in the velocity dispersion at the nucleus, this is observed in only 3-4 pixels. The sampling of their optical IFS observations is $0''.7$ per fiber, while the seeing in the observations was reported to be $0''.9$. As judging from these numbers and from their Fig. 5, with their data they could not sample the structure we see in our Fig. 8 that resolves the enhanced σ bubble we have found in our maps. We note also that the regions with highest σ in our [O III] maps of Fig. 8 are seen at approximately 1 arcsec to the north-east. This is the direction where Cazzoli et al (2014) report the presence of an outflow seen in neutral gas via the observations of the NaD optical absorption feature. Their Fig. 4 shows that the outflow – observed reaching blueshifts of up to $\approx 150 \text{ km s}^{-1}$ is seen approximately between 3 and 6 arcsec, which lies beyond the borders of our FoV. Although Cazzoli et al (2014) argue that the outflow is due to feedback from star formation, our more detailed sampling of the region, suggests that the origin of the outflow may be an AGN.

In a following work, Pereira-Santaella et al (2016) used high spatial resolution ($\sim 60 \text{ pc}$) ALMA CO (2-1) observations, HST optical and near-IR images, as well as VLT/SINFONI IFS data to characterize the resolved outflow in IRAS 11506, finding that the ALMA observations revealed a number of cold molecular gas knots along the direction of the outflow seen in neutral gas by Cazzoli et al (2014). They concluded that an extremely obscured nuclear starburst produces the outflow. We favor instead the presence of a faint/recently born AGN at the nucleus due to the resolved structure of the 240 pc bubble and enhanced line ratios correlated with the radio structure.

One possible scenario to reconcile the above results with ours is that we are probing the nuclear region which is revealing a new ejection of a plasma bubble that is pushing the surrounding gas, thus increasing its velocity dispersion. Mostly shocks but possibly also some escape of AGN radiation could then explain the increase in the emission-line ratios seen in Fig. 6. A new ejection towards the north-east may also be occurring, which could explain the increased velocity dispersion towards this direction (Kharb et al. 2017).

4.4.2 Comparison with our previous studies of OH Megamaser galaxies

In the first paper of this series of multiwavelength studies of OHM galaxies, Sales et al (2015) presented a study of IRAS 16399-0937 which is characterized as a mid to advanced merger with two nuclei embedded in a diffuse envelope. The nuclei are separated by 3.4 kpc and the spectral energy distribution revealed that the northwestern nucleus hosts a dust embedded AGN of luminosity $L_{bol} \approx 10^{44}$ erg s⁻¹.

In the second study, Hekatelyne et al (2018a) used GMOS-IFU, HST and VLA data of IRAS 23199+0123, which is an interacting pair of galaxies separated by 24 kpc. We were able to detect a Seyfert 1 nucleus in the western member of the pair revealed by the presence of an unresolved broad H α line. From the VLA data we were able to report a new maser detection, determine the position of the masers and conclude that the masers sources are correlated to shocks driven by AGN outflows.

The third study was performed for IRAS 03056+2034 (Hekatelyne et al 2018b), a barred spiral galaxy with irregular structures that could indicate a past interaction and also reveals a circumnuclear ring of star-forming regions and flocculent spiral arms. The BPT diagram and VLA data suggest the presence of an embedded AGN in the midst of by star-forming regions surrounding the nucleus.

The fourth study was on IRAS 17526+3253 (Sales et al 2019). This galaxy is in mid-stage major merger with the nuclei separated by ≈ 8.5 kpc that hosts both OH and H₂O masers. There is no strong evidence of the presence of an AGN, although this possibility can not be excluded based on the analysis of the presented data.

And finally, here we presented a study for IRAS 11506-3851, which is an isolated spiral galaxy that does not show clear signs of interaction, but shows a double-barred structure. As in the other galaxies, star-forming regions surround the nucleus. Moreover, the analysis of the VLA data, BPT diagrams and gas kinematics suggest the presence of a weak AGN immersed in a region dominated by star formation.

In summary, in the 5 OHM galaxies studied so far, the most common pattern is the presence of plenty of star-forming regions. Three are clear mergers, and in two of them we clearly find an AGN. The other two seem to be isolated galaxies, but both are barred, with one of them showing asymmetries that could be related to a past merger. Both show signatures of an embedded AGN in the midst of star-forming regions surrounding the nucleus.

We note that, although the conventional thinking is that the megamaser relates to starburst activity, our on-going observations of OHM galaxies show that the megamaser can also be related to the presence of AGN activity. We aim to

investigate a possible relation between the luminosity of the megamaser and that of the AGN, but our sample of 5 galaxies is still small for this. The AGN-related luminosities we have so far for all the targets are the megamaser and the H α luminosities, with the caveat that it is not easy to separate the H α luminosity of the AGN from that of the surrounding star formation, that is probably “contaminating” the central H α luminosity. The only significant trend is that the weakest Maser observed so far is in IRAS 11506, which also has the lowest nuclear H α luminosity of the sample we have observed.

5 CONCLUSIONS

We have performed a multiwavelength data analysis of the OHM galaxy IRAS 11506-3851 comprising HST and VLA images and GMOS-IFU spectroscopy. The GMOS-IFU observations cover the inner 6.7×9.6 kpc² at a spatial resolution of 193 pc and spectral resolution of 1.8 Å. Our main conclusions are:

- The HST images reveal an isolated spiral galaxy that combined with the GMOS-IFU observations allowed us to identify a partial circumnuclear ring of star formation with ≈ 500 pc radius and an obscured region to the north-east of the nucleus.
- From the diagnostic diagrams we show increased gas excitation internal to the star-forming ring, within a radius of 240 pc from the nucleus, due to a mixed contribution of Starburst and AGN excitation, apparently mostly due to shocks, while the excitation in the rest of the FoV, dominated by the 500 pc ring, is due to Starbursts.
- The VLA images reveal a steep spectrum kpc-scale radio source co-spatial with the 240 pc radius region of enhanced excitation that we attribute to a plasma bubble emitted by a faint AGN.
- The VLA data radio core spectral index is compatible with an AGN and the elongation observed in the spectral index map makes the radio core in this galaxy to resemble more an AGN than a nuclear Starburst.
- The residuals of the fit of a rotating-disc model to the gas kinematics reveal mild non-circular motions suggesting an outflow within the inner 240 pc co-spatial to one previously seen in neutral gas. Moreover, the whole region presents higher velocity dispersion than the surroundings, that are co-spatial with the radio emission. The enhanced velocity dispersion at the borders of this region, co-spatial with regions of increased excitation suggest shock excitation by the plasma bubble presumably emitted by a nuclear AGN.
- From the H α fluxes we estimated physical properties of the star forming regions of the 500 pc ring. The masses of ionized gas are in the range of $(0.1 - 0.8) \times 10^4 M_{\odot}$. The ionizing photons rate $\log(Q[H^+])$ is in the range 50.31 - 51.01 (units of photons s⁻¹) and the average star formation rate is about $0.005 M_{\odot} \text{yr}^{-1}$.

We argue that our observations of this OHM galaxy is unveiling the ejection of a plasma bubble that is pushing the surrounding gas and either shocks and ionizing photons from a faint AGN can explain the increased excitation of the region. We thus suggest that the origin of the outflows

previously reported in neutral and molecular gas could be this AGN.

This is the fifth OHM galaxy from a sample of 15 that we analyse using similar data, whose unresolved nuclear gas emission was known to be dominated by star formation. And is the fourth one for which GMOS-IFU data has resolved the presence of a previously unknown AGN at the nucleus. These results support the hypothesis that OHM galaxies harbor faint AGN being triggered by recent accretion of matter to their central SMBH.

ACKNOWLEDGEMENTS

This work is based on observations obtained at the Gemini Observatory, which is operated by the Association of Universities for Research in Astronomy, Inc., under a cooperative agreement with the NSF on behalf of the Gemini partnership: the National Science Foundation (United States), National Research Council (Canada), CONICYT (Chile), Ministerio de Ciencia, Tecnología e Innovación Productiva (Argentina), Ministério da Ciência, Tecnologia e Inovação (Brazil), and Korea Astronomy and Space Science Institute (Republic of Korea). This research has made use of NASA's Astrophysics Data System Bibliographic Services. This research has made use of the NASA/IPAC Extragalactic Database (NED), which is operated by the Jet Propulsion Laboratory, California Institute of Technology, under contract with the National Aeronautics and Space Administration. Support for programme HST-SNAP 11604 was provided by NASA through a grant from the Space Telescope Science Institute, which is operated by the Association of Universities for Research in Astronomy, Inc., under NASA contract NAS 5-26555. RAR thanks support from Conselho Nacional de Desenvolvimento Científico e Tecnológico (202582/2018-3, 304927/2017-1 and 400352/2016-8) and Fundação de Amparo à pesquisa do Estado do Rio Grande do Sul (17/2551-0001144-9 and 16/2551-0000251-7). CH thanks CAPES for financial support.

DATA AVAILABILITY

The GEMINI data used in this work is publicly available online via the GEMINI archive <https://archive.gemini.edu/searchform/>, with project code GS-2014A-Q-75. The VLA data is available at <https://science.nrao.edu/facilities/vla/archive> and project codes are AB660 and AL508. Finally, the HST data is available at <https://archive.stsci.edu/hst/> with project code 11604. The maps produced from these data can be shared on reasonable request to the corresponding author.

REFERENCES

Allen, M. G., Groves, B. A., Dopita, M. A., Sutherland, R. S. and Kewley, L. J., 2008, *ApJS*, 178, 20
 Allington-Smith, J. et al. 2002, *PASP*, 114, 892.
 Arribas, S., Colina, L., Bellocchi, E., Maiolino, R., & Villar-Martin, M. 2014, *A&A*, 568, A14
 Baldwin, J. A., Phillips, M. M., Terlevich, R., 1981, *PASP*, 93, 5
 Barnes, J. E., & Hernquist, L. 1992, *ARA&A*, 30, 705

Bellocchi, E., Arribas, S., Colina, L., & Miralles-Caballero, D., 2013, *A&A*, 557, A59
 Bellocchi, E., Arribas, S., & Colina, L. 2016, *A&A*, 591, A85
 Bertola, F., Bettoni, D., Danziger, J., Sadler, E., Sparke, L., de Zeeuw, T., 1991, *ApJ*, 373, 369
 Bontempi, P.; Giroletti, M., Panessa, F., Orienti, M., Doi, A., 2012, *MNRAS*, 426, 588
 Bruzual, G.; Charlot, S., 2003, *MNRAS*, 344, 1000.
 Brum, C., Riffel, R. A., Storch-Bergmann, T., Robinson, A., Schnorr Muller, A., Lena, D., 2017, *MNRAS*, 469, 3405.
 Cappellari, M., & Emsellem, E. 2004, *PASP*, 116, 138
 Cappellari, M., 2017, *MNRAS*, 466, 798.
 Cazzoli, S., Arribas, S., Maiolino, R., & Colina, L. 2016, *A&A*, 590, A125
 Cazzoli, S., Arribas, S., Colina, L., et al. 2014, *A&A*, 569, A14
 Cicone, C., Maiolino, R., Sturm, E., et al. 2014, *A&A*, 562, A21
 Darling J., Giovanelli R., 2002, *ApJ*, 572, 810
 Freitas, I. C. et al., 2018, *MNRAS*, 476, 2760
 Galliano, E., & Alloin, D. 2008, *A&A*, 487, 519
 Greusard, D., Friedli, D., Wozniak, H., Martinet, L., & Martin, P. 2000, *A&AS*, 145, 425
 Haan, S., Surace, J. A., Armus, L., et al. 2011, *AJ*, 141, 100
 Hekatelyne, C., Riffel, R. A., Sales, D., Robinson, A., Gallimore, J., Storch-Bergmann, T., Kharb, P., O'Dea, C. Baum, S., 2018a *MNRAS*, v. 474, p. 5319
 Hekatelyne, C., Riffel, R. A., Sales, D., Robinson, A., Storch-Bergmann, T., Kharb, P., Gallimore, J., Baum, S., O'Dea, C., 2018b, *MNRAS*, v. 479, p. 3966
 M. G. Hennig, Riffel, R. A., Dors O. L., Riffel, R., Storch-Bergmann, T., Colina, L., *MNRAS*, 2018, 477, 1086
 Hopkins, P. F., Hernquist, L., Cox, T. J., et al. 2006, *ApJS*, 163, 1
 Hopkins, P. F., Quataert, E., & Murray, N. 2012, *MNRAS*, 421, 3522
 Kauffmann, G. et al. 2003a, *MNRAS*, 346, 1055
 Kennicutt, R. C. 1998, *ARA&A*, 36, 189
 Kharb, P.; Hota, Ananda; Croston, J. H.; Hardcastle, M. J.; O'Dea, C. P., Kraft, R. P., Axon, D. J., Robinson, A., 2010, *ApJ*, 723, 580
 Kharb, P.; Subramanian, S.; Vaddi, S.; Das, M.; Paragi, Z., 2017, *ApJ*, 846, 12
 Kennicutt, R. C. 1998, *ARA&A*, 36, 189
 Kewley, L. J., Dopita, M. A., Sutherland, R. S., Heisler, C. A., Trevena, J. 2001a, *ApJ*, 556, 121
 Lo K. Y., 2005, *ARA&A*, 43, 625
 Markwardt C. B., 2009, in Bohlender D. A., Durand D., Dowler P., eds, *ASP Conf. Ser. Vol. 411, Astronomical Data Analysis Software and Systems XVIII*. Astron. Soc. Pac., San Francisco, p. 251
 Nelson, D., Genel, S., Vogelsberger, M., et al. 2015, *MNRAS*, 448, 59
 Norris, R. P., Whiteoak, J. B., Gardner, F. F., Allen, D. A., & Roche, P. F. 1986, *MNRAS*, 221, 51P
 Orienti, M., Prieto, M. A., 2010, *MNRAS*, 401, 2559
 Osterbrock, D. E., 1989, *Astrophysics of Gaseous Nebulae and Active Galactic Nuclei*, University Science Books, Mill Valley, California
 M. Pereira-Santaella, L. Colina, S. Garcia-Burillo, A. Alonso-Herrero, S. Arribas, S. Cazzoli, B. Emonts, J. Piqueras Lopez, P. Planesas, T. Storch-Bergmann, A. Usero, and M. Villar-Martin, 2016, *A&A*, 594, A81
 M. Pereira-Santaella, L. Colina, S. Garcia-Burillo, F. Combes, B. Emonts, S. Aalto, A. Alonso Herrero, S. Arribas, C. Henkel, A. Labiano, S. Muller, J. Piqueras Lopez, D. Rigopoulou, and P. van der Werf, 2018, *A&A*, v.616, A171
 Peterson B. M., 1997, *An Introduction to Active Galactic Nuclei*, Cambridge, New York Cambridge University Press
 Riffel, Rogemar A., Storch-Bergmann, T., Dors, O. L., Winge,

- C., 2009, MNRAS, 393, 783
- Riffel R. A., 2010, ApSS, 327, 239
- Riffel, Rogemar A., Colina, L., Storchi-Bergmann, T., Piqueras, López J., Arribas, S., Riffel, R., Pastoriza, M., Sales, Dinalva A., Dametto, N. Z., Labiano, A. & Davies, R. I., 2016, MNRAS, 461, 4192.
- Roy, A. L., Wilson, A. S., Ulvestad, J. S., Colbert, J. M., 2000, EVN Symposium 2000, Proceedings of the 5th european VLBI Network Symposium
- Sanders, D. B., Soifer, B. T., Elias, J. H., et al. 1988a, ApJ, 325, 74
- Sanders, D. B., Mirabel, I. F., 1996, ARA&A, 34, 749.
- Sadler, Elaine M., Slee, O. B., Reynolds, J. E., Roy, A. L., 1995, MNRAS, 276, 1373
- Sales, D. A., Robinson, A., Axon, D. J., et al., 2015, ApJ, 799, 25
- Sales, D., Robinson, A., Riffel, R. A, Storchi-Bergmann, T, Galimore, J F, Kharb, P, Baum, S, O’dea, C, Hekatelyne, C, Ferrari, F., 2019, MNRAS, v. 486, 3350
- Soifer, B. T., Sanders, D. B., Madore, B. F., Neugebauer, G., Danielson, G. E., Elias, J. H., Lonsdale, C. J., Rice, W. L., 1987, ApJ, 320, 238.
- Storchi-Bergmann, T. & Schnorr-Müller, A 2019, Nature Astronomy, 3, 48
- Schaye, J., Crain, R. A., Bower, R. G., et al. 2015, MNRAS, 446, 521
- Tody, D. 1986, The IRAF Data Reduction and Analysis System in Proc. SPIE Instrumentation in Astronomy VI, ed. D.L. Crawford, 627, 733
- Tody, D. 1993, IRAF in the Nineties” in Astronomical Data Analysis Software and Systems II, A.S.P. Conference Ser., Vol 52, eds. R.J. Hanisch, R.J.V. Brissenden, J. Barnes, 173.
- van den Broek, A. C., van Driel, W., de Jong, T., et al. 1991, A&AS, 91, 61
- van der Kruit, P.C., Allen, R.J., 1978, ARA&A, 16, 103
- Wold, M., Galliano, E., 2006, MNRAS, 369, 47.

This paper has been typeset from a $\text{\TeX}/\text{\LaTeX}$ file prepared by the author.